

**Orientation and Size Dependent Mechanical Modulation  
within Individual Secondary Osteons in Cortical Bone Tissue**

Journal:	<i>Journal of the Royal Society Interface</i>
Manuscript ID:	rsif-2012-0953.R1
Article Type:	Research
Date Submitted by the Author:	n/a
Complete List of Authors:	Carnelli, Davide; Politecnico di Milano, ; Massachusetts Institute of Technology, Vena, Pasquale; Politecnico di Milano, ; IRCCS, Istituto Ortopedico Galeazzi, Dao, Ming; Massachusetts Institute of Technology, Ortiz, Christine; Massachusetts Institute of Technology, Contro, Roberto; Politecnico di Milano,
Subject:	Biomechanics < CROSS-DISCIPLINARY SCIENCES
Keywords:	hierarchical structure, anisotropy, length scale effect, nanoindentation, secondary osteons

SCHOLARONE™  
Manuscripts

1  
2  
3 **Orientation and Size Dependent Mechanical Modulation within Individual Secondary**  
4 **Osteons in Cortical Bone Tissue**  
5  
6  
7  
8

9 Davide Carnelli<sup>1,3,δ</sup>, Pasquale Vena<sup>2,4</sup>, Ming Dao<sup>3</sup>, Christine Ortiz<sup>3</sup>, and Roberto Contro<sup>1</sup>  
10  
11

12  
13  
14 <sup>1</sup> LaBS-Laboratory of Biological Structure Mechanics, Department of Structural Engineering,  
15 Politecnico di Milano, P.zza L. da Vinci 32, 20133, Milan, Italy.  
16

17  
18 <sup>2</sup> LaBS-Laboratory of Biological Structure Mechanics, Chemistry, Material and Chemical  
19 Engineering Department, Politecnico di Milano, P.zza L. da Vinci 32, 20133, Milan, Italy.  
20

21  
22 <sup>3</sup> Department of Materials Science and Engineering, Massachusetts Institute of Technology,  
23 77 Massachusetts Avenue, 02139, Cambridge, MA, USA.  
24

25  
26 <sup>4</sup> IRCCS, Istituto Ortopedico Galeazzi, P.zza R. Galeazzi 4, 20161, Milano, Italy  
27

28  
29 <sup>δ</sup> Current Address: Complex Materials, Department of Materials, ETH Zürich, Wolfgang-  
30 Pauli-Str. 10, 8093 Zürich, Switzerland  
31  
32  
33

34  
35  
36 **Address for correspondence:**  
37

38 Dr. Davide Carnelli  
39

40 Complex Materials  
41

42 Department of Materials  
43

44 ETH Zürich  
45

46 Wolfgang-Pauli-Str. 10, 8093 Zürich  
47

48 Switzerland  
49

50 Phone: +41 44 633 0495  
51

52 Fax: +41 44 632 1101  
53

54 e-mail: [davide.carnelli@mat.ethz.ch](mailto:davide.carnelli@mat.ethz.ch)  
55  
56  
57  
58  
59  
60

## SUMMARY

Anisotropy is one of the most peculiar aspects of cortical bone mechanics; however, its anisotropic mechanical behavior should be treated only with strict relationship to the length scale of investigation.

In this study, we focus on quantifying the orientation and size dependence of the spatial mechanical modulation in individual secondary osteons of bovine cortical bone using nanoindentation. Tests were performed on the same osteonal structure in the axial (along the long bone axis) and transverse (normal to the long bone axis) directions along arrays going radially out from the Haversian canal at four different maximum depths on three secondary osteons.

Results clearly show a periodic pattern of stiffness with spatial distance across the osteon. The effect of length scale on lamellar bone anisotropy and the critical length at which homogenization of the mechanical properties occurs were determined. Further, a laminate-composite based analytical model was applied to the stiffness trends obtained at the highest spatial resolution to evaluate the elastic constants for a sub-layer of mineralized collagen fibrils within an osteonal lamella on the basis of the spatial arrangement of the fibrils.

The hierarchical arrangement of lamellar bone is found to be a major determinant for modulation of mechanical properties and anisotropic mechanical behavior of the tissue.

Keywords: hierarchical structure; anisotropy; length scale effect; nanoindentation; secondary osteons.

## 1 INTRODUCTION

Cortical bone is a heterogeneous, hierarchical composite material with important structural features spanning multiple length scales, each of which contributes to macroscopic biomechanical function [1-5]. At the microstructural level, both in humans and in many other large vertebrates, a particularly critical determinant of the mechanical properties of the whole tissue are concentric lamellar cylindrical structures called secondary osteons (Fig. 1 A-C) [6, 7].

The detailed lamellar structure within individual secondary osteons was interrogated via synchrotron X-ray texture measurements and consists of three-dimensional helicoids of mineralized collagen fibrils [6]. Transmission electron microscopy (TEM) [7-10] revealed that the mineralized collagen fibrils that make up one sub-layer of the lamellar unit have an internal crystalline structure. Within each lamella, which typically has a  $\sim 3-7 \mu\text{m}$  thickness, the long axis of the collagen fibrils rotates from a direction roughly parallel to the osteonal axis at one lamellar boundary (referred to as “thick” sub-layers or sub-lamellae,  $\sim 2-4 \mu\text{m}$  thick) to a direction approximately perpendicular to it at the opposite lamellar boundary (referred to as “thin” sub-layers or sub-lamellae,  $\sim 1-2 \mu\text{m}$  thick).

The mechanical characterization of individual osteons was performed in tension, compression, and torsion [11-13], as well as with ultrasound [14]. Instrumented indentation was also applied to evaluate the elastic properties of lamellar bone within the osteonal structure along multiple orientations [15-17]. These studies identified anisotropic elasticity of individual osteons, where the axial direction was stiffer than the transverse direction with an anisotropic ratio (axial/transverse) of  $\sim 1.5$ , similar to the value found for macroscopic cortical bone [2, 3] and lower than the expected value for individual mineralized collagen fibrils ( $\sim 2.0$ ) [18].

1  
2  
3 Considering the hierarchical structural features of bone [6], different characteristic  
4 sizes which may also play functional roles in bone exist at different length scales [19-21]. In  
5 a recent study, Yao et al. [21] adopted AFM-based nanoindentation to identify a  
6 characteristic length scale of approximately 200 nm within one sub-layer of the lamellar unit;  
7 at a higher level, spatially-controlled nanoindentation experiments within individual osteons  
8 allowed Gupta et al. [19] to identify a larger characteristic length scale due to the periodicity  
9 of the osteonal lamellae, with thicker sub-lamellae of higher stiffness alternating with thinner  
10 sub-lamellae of lower stiffness. The spatial variation of indentation modulus within a lamella  
11 was attributed to the rotation of the inherently anisotropic collagen fibrils [19, 22] and  
12 variations in the mineral content [19]. Nevertheless, an experimentally validated analytical  
13 model that directly links the nanoscale rotational arrangements of collagen fibrils and the  
14 corresponding anisotropic elasticity is still missing.  
15  
16  
17  
18  
19  
20  
21  
22  
23  
24  
25  
26  
27  
28

29  
30 In this study, we focus on quantifying the orientation and size dependence of the  
31 spatial mechanical modulation in individual secondary osteons of bovine cortical bone using  
32 nanoindentation. Experiments were carried out in two orthogonal orientations within the  
33 same individual osteon. Tests were performed at four different maximum penetration depths  
34 to study the effect of indentation area on mechanical modulation. An analytical model which  
35 assumes the inherent anisotropy of the mineralized collagen fibrils as well as their orientation  
36 was introduced to estimate the elastic constants of a sub-layer of mineralized collagen fibrils.  
37  
38  
39  
40  
41  
42  
43  
44  
45  
46

## 47 **2 MATERIALS AND METHODS**

48  
49 In the following, the Haversian canal axis is referred to as the “Axial” direction (A), while the  
50 plane perpendicular to this axis is referred to as the “Transverse” direction ( $T_1$ ,  $T_2$ ). Similarly,  
51 the long axis of the mineralized collagen fibrils is herein referred to as the “Longitudinal”  
52 direction (L), while the plane perpendicular to this axis is referred to as the “Perpendicular”  
53  
54  
55  
56  
57  
58  
59  
60

1  
2  
3 direction ( $P_1, P_2$ ). Thus,  $A, T_1, T_2$  represents a global coordinate system based on the whole  
4  
5 secondary osteon; whereas,  $L, P_1, P_2$  represents a local coordinate system related to the  
6  
7 mineralized collagen fibrils.  
8

9  
10 2.1 Sample preparation and characterization. Samples were kept under conditions close  
11  
12 to the physiological one until the tests; to this purpose no alcohol dehydration, freezing,  
13  
14 embedding, thermal drying, long-term storage in ambient conditions, or chemical fixation  
15  
16 were used. Adult lamellar bone obtained from a 30-month old cow was harvested from  
17  
18 between the tibial metaphysis and diaphysis. Approximately 5 mm cubic specimens were  
19  
20 obtained by using a diamond-impregnated annular wafering saw (Isomet 5000, Buehler, Inc.,  
21  
22 Lake Bluff, IL, USA) running at 400–600 rpm under constant water irrigation. In order to  
23  
24 expose the osteons' Haversian canal, the first two cuts were performed along the transverse  
25  
26 direction and the second ones along the axial directions. The samples were then polished  
27  
28 using a metallographic polishing wheel and adhesive papers with successively smaller  $Al_2O_3$   
29  
30 particle grit sizes. Samples were rinsed copiously with deionized (DI) water followed by  
31  
32 ultrasonication in DI water between polishing intervals. The cutting and polishing procedures  
33  
34 were performed the day after harvesting.  
35  
36  
37

38  
39 From optical (Nikon Eclipse L150, Fig. 1 A-B) and scanning electron microscopy  
40  
41 (JEOL SEM 6320FV, Fig. 1 C), the average osteonal diameter was found to be  $\sim 200 \mu m$  and  
42  
43 the average thickness of the first 4-5 individual lamellae around the Haversian canal is  
44  
45  $5.01 \pm 0.10 \mu m$ . Contact mode atomic force microscope (AFM, MFP-3D, Asylum Research,  
46  
47 Inc., Santa Barbara, CA, USA) imaging was performed to assess the RMS surface roughness  
48  
49 achieved with the polishing procedure, which was quantified as  $6.0 \pm 0.7 \text{ nm}$  on several  $2 \times 2$   
50  
51  $\mu m$  areas in different locations on the three osteonal structures.  
52  
53  
54  
55  
56  
57  
58  
59  
60

1  
2  
3 Finally, samples were fixed into the groove of a home-built sample holder which  
4 allows for mechanical testing of the same osteonal structure in different directions with  
5 respect to the osteonal axis (Fig. 1 D-E).  
6  
7  
8

9  
10 2.2 Nanoindentation experiments. All instrumented indentation experiments were  
11 conducted in the osteonal region of cortical bone shortly after harvesting and over a short  
12 enough time period so that no significant modification of the sample state was ensured; to  
13 this purpose the statistical invariance of experimental data over time (the whole time span of  
14 the testing period) was checked (data not shown). The effect of hydration state was neglected  
15 at this stage, as the bone samples were tested in ambient conditions (20°C and 50% relative  
16 humidity). A Triboindenter (Hysitron, Inc., Minneapolis, MN, USA) was employed with a  
17 Berkovich diamond tip. The tip area function and machine compliance were calibrated on a  
18 fused silica reference sample by performing 100 indentations between 100 to 10000  $\mu\text{N}$   
19 maximum forces [23].  
20  
21  
22  
23  
24  
25  
26  
27  
28  
29  
30

31  
32 Experiments were performed in displacement control along arrays going radially out  
33 from the Haversian canal edge to the external region of the osteon at four different maximum  
34 depths: 50, 100, 200 and 300 nm. The experimental procedure is detailed in Table 1. The  
35 displacement rates of the indentation experiments were 20 nm/s and 100 nm/s in the loading  
36 and unloading branches of the indentation curve, respectively. An automatic preliminary  
37 thermal drift correction was applied before each indentation. Preliminary investigations were  
38 performed to ensure that time-dependent effects were minimal (see [24] for further details).  
39 This experimental procedure was employed on three secondary osteons in both the axial and  
40 transverse directions (A and T<sub>1</sub>, respectively, in Fig. 1 A-E). A total of ~2000 indentations  
41 were carried out.  
42  
43  
44  
45  
46  
47  
48  
49  
50  
51  
52  
53  
54  
55  
56  
57  
58  
59  
60

The Oliver-Pharr method [25] was adopted to obtain the indentation modulus  $M$  from the unloading portion of each test. An unloading segment range between 95% and 40% of maximum load was chosen for data fitting.

2.3 Empirical formulation for stiffness modulation. The oscillatory function:

$$M(r) = \frac{\Delta M}{2} \cdot \sin\left(\frac{2\pi r}{w} + c\right) + M_0 \quad (1)$$

was adopted to fit the stiffness modulation along the indentation paths. In Eq. (1),  $r$  is the radial position across the osteon,  $r=0$  being the Haversian canal inner edge;  $w$  is the mean value of the experimentally observed lamellar width (5.01  $\mu\text{m}$ );  $\Delta M$  is the oscillatory function amplitude;  $M_0$  is its mean value.

2.4 Anisotropic analytical models. The spatial modulation of stiffness at the lowest maximum indentation depth probed (50 nm) was fitted to an analytical model which assumes the inherent anisotropy of the mineralized collagen fibrils and allows for the evaluation of the effective stiffness of the sub-lamellae as a function of collagen fibril orientation. The orientation dependent uniaxial Young's modulus  $E$  of an individual sub-lamella was obtained by applying the rotation formula [19, 26, 27]:

$$E(\theta) = \left[ \frac{\cos^4(\theta)}{E_L} + \frac{\sin^4(\theta)}{E_P} + \left( \frac{1}{G_{LP}} - 2 \frac{\nu_{LP}}{E_L} \right) \cos^2(\theta) \sin^2(\theta) \right]^{-1} \quad (2)$$

where  $\theta$  is the angle between the long axis of the mineralized collagen fibrils (longitudinal direction, L) and the loading direction,  $E_L$  is the uniaxial Young's modulus along the mineralized collagen fibrils long axis direction (longitudinal direction, L),  $E_P$  is the uniaxial Young's modulus perpendicular to the mineralized collagen fibril axis (perpendicular directions,  $P_1$  and  $P_2$ ),  $G_{LP}$  is the shear modulus and  $\nu_{LP}$  is the Poisson's ratio. The model assumes that individual collagen fibrils and uniformly oriented planar layers of fibrils are transversely isotropic ( $P_1=P_2=P$ ) [28-30].



The uniaxial Young's moduli were directly estimated from the experimental nanoindentation loading-unloading curves by employing the analytical model for anisotropic elastic contact introduced by Delafargue and Ulm [31]. This model relates the indentation moduli of the mineralized collagen fibril sub-lamellae in the longitudinal (L) and perpendicular ( $P_1$ ,  $P_2$ ) directions to the material stiffness tensor coefficients for individual collagen fibril layers ( $C_{ijkh}=C_{ijkh}(E_L, E_P, G_{PL}, \nu_{LP}, \nu_{PP})$ ,  $\nu_{PP}$  being the Poisson's ratio in the isotropy plane). The model holds for transversely isotropic and orthotropic solids under rigid conical indentation along the three principal material symmetry directions. For a transversely isotropic material model, the indentation modulus  $M$  in the axis of symmetry direction (here named as direction 3, corresponding to the longitudinal collagen fibril axis direction L) is explicitly related to  $C_{ijkh}$  with the following expression:

$$M_3 = 2 \sqrt{\frac{C_{1111}C_{3333} - C_{1133}^2}{C_{1111}} \cdot \left( \frac{1}{C_{2323}} + \frac{2}{\sqrt{C_{1111}C_{3333} + C_{1133}}} \right)^{-1}} \quad (3)$$

For the indentation directions normal to the axis of symmetry (directions 1 and 2, corresponding to the perpendicular collagen fibril axes  $P_1=P_2=P$ ), the indentation moduli  $M_1, M_2$  are as follows:

$$M_1 = M_2 \approx \sqrt{\frac{C_{1111}^2 - C_{1122}^2}{C_{1111}} \cdot \left( \frac{C_{1111}}{C_{3333}} \right)^{1/2}} \cdot M_3 \quad (4)$$

The above formulae were applied at those indentation locations for which indentation direction is assumed to be aligned with a principal material direction (i.e. in the case of indentation of thick and thin sub-lamellae). Using the indentation moduli  $M_1$  and  $M_3$  calculated from nanoindentation data via the Oliver-Pharr method, Eqs. (3-4) were solved for  $E_L$  and  $E_P$ . The Poisson's ratios  $\nu_{LP}, \nu_{PP}$  were assumed according to literature data ([18], see Eq. (6)) and the shear modulus  $G_{LP}$  was related to the remaining parameters (see Eq. (6)).

For validation purposes, the Swadener-Pharr method [32] was employed to compute the indentation moduli  $M$  in all the directions of the space for a given stiffness tensor  $\mathbf{C}$ , as obtained from the solutions of Eqs. (2-4):

$$M = \frac{4\pi}{\int_0^{2\pi} \frac{\mathbf{B}^{-1}(\mathbf{t}(\gamma), \mathbf{C}) : [\mathbf{a}_3 \otimes \mathbf{a}_3]}{\sqrt{(a_1/a_2)\cos^2 \gamma + (a_1/a_2)\sin^2 \gamma}} d\gamma} \quad (5)$$

In this formulation,  $\mathbf{B}$  is the Barnett-Lothe tensor related to stiffness tensor  $\mathbf{C}$ ;  $(\mathbf{r}, \mathbf{s}, \mathbf{t})$  is an orthogonal reference system;  $(\mathbf{a}_1, \mathbf{a}_2, \mathbf{a}_3)$  is the indentation coordinate system;  $\gamma$  is the angle between the direction  $\mathbf{t}$  and the  $\mathbf{a}_1$  axis;  $a_1$  and  $a_2$  are the semi-axes lengths of the elliptical projected area of contact.

### 3 RESULTS

3.1 Mechanical modulation at the lamellar level. The average loading-unloading indentation curves obtained in the two orthogonal directions at the four maximum penetration depths are reported in Fig. 2. The curves show how the indentation response of the tissue depends on the global orientation direction (A vs. T). A good repeatability of the loading branch for increasing loads was obtained between tests at different maximum depth. The mean value and standard deviation of maximum load at 50, 100, 200, and 300 are 107 ( $\pm 10$ )  $\mu\text{N}$ , 326 ( $\pm 29$ )  $\mu\text{N}$ , 1004 ( $\pm 69$ )  $\mu\text{N}$ , and 1984 ( $\pm 104$ )  $\mu\text{N}$ , respectively, in the axial direction, and 110 ( $\pm 19$ )  $\mu\text{N}$ , 263 ( $\pm 29$ )  $\mu\text{N}$ , 648 ( $\pm 77$ )  $\mu\text{N}$ , and 1354 ( $\pm 218$ )  $\mu\text{N}$ , respectively, in the transverse direction. The corresponding COV (coefficient of variation, defined as the ratio between the standard deviation and the mean value) ranges between  $\sim 0.17$  (at 50 nm maximum depth, transverse direction) and  $\sim 0.05$  (at 300 nm maximum depth, axial direction). The tissue indentation modulus ranges from 26.24 ( $\pm 1.68$ ) GPa to 19.73 ( $\pm 0.73$ ) GPa in the axial direction and from 23.59 ( $\pm 3.55$ ) GPa to 15.39 ( $\pm 1.04$ ) GPa in the transverse

1  
2  
3 direction. The corresponding COV ranges between  $\sim 0.15$  (at 50 nm maximum depth,  
4 transverse direction) and  $\sim 0.04$  (at 300 nm maximum depth, axial direction).  
5  
6

7  
8 The indentation modulus  $M$  shows a periodic alternating trend of stiffness with spatial  
9 distance radially across the osteon for both the axial (Fig. 3) and transverse (Fig. 4)  
10 directions, consistent with results reported in [19]. The coefficient of determination ( $R^2$ ) for  
11 fits of the experimental data (Figs. 3-4) to Eq. (1) ranged between 0.61 and 0.01. Higher  
12 correlations were found for data taken at the smaller depths (50 nm), while smaller values  
13 corresponded to indentations carried out at 300 nm depths in both directions. All the obtained  
14  $R^2$  values are reported in the caption of Figs. 3-4. Further, a power analysis has been carried  
15 out on the data of Figs. 3-4. A statistically significant difference (one-way ANOVA,  
16  $p < 0.001$ ) was found between the peaks and the valleys of the modulation at 50 and 100 nm  
17 maximum depth in both the axial and transverse direction, as well as for the 200 nm, axial  
18 direction experiments ( $p < 0.05$ ). Instead, no statistically significant difference ( $p > 0.05$ ) was  
19 found at 200 nm maximum depth in the transverse direction and at 300 nm maximum depth.  
20  
21  
22  
23  
24  
25  
26  
27  
28  
29  
30  
31  
32  
33

34 The mean value,  $M_0$ , and the amplitude of the modulation,  $\Delta M$ , depend on maximum  
35 depth and orientation of the indentation tests (Fig. 5). The mean values  $M_0$  show the tissue to  
36 be stiffer when loaded in the axial direction compared to the transverse direction (Fig. 5A):  
37 indeed, anisotropy ratios, calculated as axial vs. transverse indentation moduli mean values,  
38 vary between  $\sim 1.1$  at lower maximum indentation depths (50 and 100 nm) to  $\sim 1.3$  at higher  
39 maximum indentation depths (200 and 300 nm). Simultaneously, the spatial modulation of  
40 the mechanical properties is higher in the transverse compared to the axial direction (i.e.  
41 higher  $\Delta M$ , Fig. 5B). A decrease in the indentation moduli mean values is observed between  
42 50 and 200 nm maximum depths, this decay being more pronounced in the transverse ( $\sim 35\%$ )  
43 than in the axial ( $\sim 22\%$ ) direction. Instead, no statistically significant difference (one-way  
44 ANOVA,  $p > 0.05$ ,  $n=9$ ) is noticeable within the same direction between 200 and 300 nm (Fig.  
45  
46  
47  
48  
49  
50  
51  
52  
53  
54  
55  
56  
57  
58  
59  
60

5A). The amplitude of the stiffness modulation (Fig. 5B) decreases with the indentation depth as well. The transverse amplitude is approximately two times higher than the axial at 50 nm indentation depth, while the trends in the two directions are similar beyond 100 nm depth: indeed, at higher indentation depths (200 and 300 nm), the amplitude values in both directions vanish and the difference between the amplitude values becomes negligible, as the two datasets show no statistically significant difference ( $p>0.05$ ,  $n=9$ ).

3.2 Estimation of  $E_L$ ,  $E_P$  and  $E(\theta)$  from the anisotropic analytical models. It is expected that carrying out indentations spatially from the Haversian canal edge to the osteonal external boundary will result in the angle  $\theta$  continuously changing along the radial path due to the spiral twisting of the mineralized collagen fibrils within a single lamella.  $E_L$  and  $E_P$  were estimated from indentation data at the lowest maximum indentation depth (50 nm, where both the spatial and depth resolution of the experiments were the highest, Figs. 3A-4A) using the Delafargue and Ulm model [31]. Since this approach is valid only in the principal material symmetry directions, the analysis was carried out at spatial locations across the osteon where the indentation loading axis was parallel and perpendicular to the mineralized collagen fibrils long axis, that is at the 9 different points  $r_i$  (with  $r_i=0, 2.5, 5, 7.5, 10, 12.5, 15, 17.5$  and  $20$   $\mu\text{m}$  radial distances from the Haversian canal edge) corresponding to the peaks and valleys of the stiffness modulation in the axial and transverse directions (Figs. 3A-4A). Thus, the indentation moduli  $M_A(r_i)$  and  $M_T(r_i)$  estimated from the Oliver-Pharr method represent the left-hand side of the system of Eqs. (3-4). In order to simultaneously calculate the uniaxial elastic moduli  $E_L(r_i)$  and  $E_P(r_i)$ , the three remaining material constants  $\nu_{PP}(r_i)$ ,  $\nu_{LP}(r_i)$  and  $G_{LP}(r_i)$  were set to:

$$\nu_{PP}(r_i) = 0.358; \quad \nu_{LP}(r_i) = 0.315; \quad G_{LP}(r_i) = \frac{E_L(r_i) + E_P(r_i)}{2} \cdot \frac{1}{2 \cdot \left(1 + \frac{\nu_{LP}(r_i) + \nu_{PL}(r_i)}{2}\right)} \quad (6)$$

1  
2  
3 Here,  $\nu_{PP}(r_i)$  and  $\nu_{LP}(r_i)$  are average values from literature ([18], see Table 3) and refer to  
4  
5 the mechanical properties of a single sub-lamella. This procedure was applied to the 9  
6  
7 couples of indentation moduli  $M_A(r_i)$  and  $M_T(r_i)$ , enabling the identification of the 9  
8  
9 corresponding couples of uniaxial elastic moduli  $E_L(r_i)$  and  $E_P(r_i)$  reported in Fig. 6A-B  
10  
11 (bars).  
12  
13

14  
15 The analytical model in Eq. (2) was then adopted to calculate  $E(\theta)$  in the axial and  
16  
17 transverse directions (Figs. 6A-B, sinusoidal curves), thus allowing the prediction of the  
18  
19 stiffness at any arbitrary angle with respect to the fibril axis for the two experimental trends.  
20  
21 In both cases, the Poisson's ratio  $\nu_{LP}$  was set to the corresponding literature values for a sub-  
22  
23 layer in an osteonal lamella found by Yoon and Cowin ([18], see Table 3); also, the  
24  
25 periodicity of the modulation was set to the experimentally observed lamellar width (5.01  
26  
27  $\mu\text{m}$ ). Results of this fitting are provided in Table 2. The small discrepancy ( $\sim 6\%$ ) in  $E_L$   
28  
29 between the axial and transverse directions means that the mineralized collagen fibrils  
30  
31 belonging to the thick and thin sub-lamellae maintain similar longitudinal mechanical  
32  
33 properties.  $E_P$  exhibited a much higher discrepancy between axial and transverse direction  
34  
35 ( $\sim 23\%$ ) indicating that the transverse properties of the mineralized collagen fibrils are  
36  
37 different in the thick and thin sub-lamellae.  
38  
39  
40  
41

42 **3.3 Elastic constants for a sub-layer within an osteonal lamella.** A set of orthotropic  
43  
44 elastic parameters for a mineralized collagen fibrils sub-layer was inferred from the previous  
45  
46 fittings by properly merging the two datasets reported in Table 2. In the proposed set of  
47  
48 elastic parameters (Table 3), the uniaxial Young's modulus  $E_L$  corresponds to the mean value  
49  
50 of the Young's moduli evaluated along the fibrils long axis in thin and thick layers; instead,  
51  
52 uniaxial Young's moduli  $E_{P1}$  and  $E_{P2}$ , as well as the shear moduli  $G_{LP1}$  and  $G_{LP2}$ , are directly  
53  
54 obtained from the previous fittings. The remaining entries of the stiffness tensor, i.e. the shear  
55  
56 modulus and the Poisson's ratio in the P<sub>1</sub>-P<sub>2</sub> plane,  $G_{P1P2}$  and  $\nu_{P1P2}$ , were taken from literature  
57  
58  
59  
60

1  
2  
3 ([18], see Table 3). For comparison purposes, the set of orthotropic elastic for a sub-layer in  
4  
5 an osteonal lamella obtained by Yoon and Cowin [18] are included in Table 3.  
6

7 3.4 Validation of the experimental and analytical procedures. In order to validate the  
8  
9 above procedure, the indentation moduli trends in the axial and transverse directions at 50 nm  
10  
11 depth were calculated through the Swadener-Pharr method [32] using the set of elastic  
12  
13 parameters reported in Table 2 (transversely isotropic model) and in Table 3 (orthotropic  
14  
15 model). The indentation moduli are computed using  $5^\circ$  spacing for  $\theta$ , corresponding to  $\sim 140$   
16  
17 nm spacing in the radial paths. The computed values, compared to the experimental measures  
18  
19 obtained at 50 nm maximum depth (Figs. 3A-4A) and the fitting to the oscillatory function of  
20  
21 Eq. (1), are shown in Fig. 7. Both material models agree reasonably well with the  
22  
23 experimental values, as evidenced by the coefficients of determination  $R^2$  (reported in Fig. 7  
24  
25 caption) ranging between 0.59 and 0.62.  
26  
27  
28  
29

30 Results from the application of the Swadener-Pharr method are also presented in  
31  
32 Tables 4-5, where the indentation moduli mean value and amplitude of the modulation  
33  
34 calculated with the oscillatory function best fitting the data (see Eq. (1)) are compared to the  
35  
36 computed mean value and amplitude of the oscillatory trends (dotted lines in Fig. 7). The  
37  
38 percentage differences between the experimental and the computed indentation values are  
39  
40 lower for the orthotropic elastic behavior (below 5%) than the transversely isotropic  
41  
42 behavior, where differences up to  $\sim 20\%$  were found. The two pieces of evidence above - i.e.  
43  
44 the fact that the coefficient of determination  $R^2$  associated to the Swadener-Pharr prediction  
45  
46 with an orthotropic material model is similar to the  $R^2$  values obtained via Eq. (1), and the  
47  
48 low discrepancy in terms of indentation moduli mean value and amplitude of the modulation  
49  
50 between the experimental and the computed data for and orthotropic model – support both the  
51  
52 reliability of the elastic parameters obtained through application of Eq. (2) to the data and the  
53  
54  
55  
56  
57  
58  
59  
60

1  
2  
3 assumption of orthotropy to model the elastic mechanical behavior of a sub-layer of  
4 mineralized collagen fibrils within an osteonal lamella.  
5  
6  
7

#### 8 9 10 **4 DISCUSSION**

11 The aim of the study was to determine the orientation and size dependent mechanical  
12 properties of individual secondary osteons in cortical bone, as well as to investigate the way  
13 the constituents' anisotropy and their arrangement in the hierarchical structure concur in the  
14 development of the anisotropic mechanical behavior of the tissue. Indentation experiments at  
15 different maximum depths showed a periodic alternating of stiffer layers with less stiff layers  
16 in which the indentation modulus mean values as well as the amplitude of the modulation  
17 depend on maximum depth and orientation of the indentation tests. A characteristic length  
18 due to the periodicity of the osteonal lamellae was quantified. Further, the elastic constants  
19 for a sub-layer of mineralized collagen fibrils within an osteonal lamella were identified from  
20 the indentation moduli by applying an analytical model which assumes inherent anisotropy of  
21 the mineralized collagen fibrils as well as their spatial arrangement.  
22  
23  
24  
25  
26  
27  
28  
29  
30  
31  
32  
33  
34  
35

36 The smallest experimental characteristic length probed (50 nm maximum depth, ~400  
37 nm contact diameter) is comparable to the size of a few mineralized collagen fibrils and  
38 allowed the evaluation of the mechanical properties of a single sub-layer of fibrils in the  
39 lamellar structure; whereas, the largest experimental characteristic length sampled (300 nm  
40 maximum depth, ~2.0  $\mu\text{m}$  contact diameter) may accommodate ~10 to 20 bunches of  
41 collagen fibrils oriented along multiple directions and, thus, involves multiple sub-layers,  
42 whose thickness can vary between few hundreds of nanometers to a couple of microns [22,  
43 33-35]. These investigations enabled the identification of a decrease in the values of  
44 indentation moduli with the penetration depth (Fig. 5A) which indicates a possible size effect  
45 in the mechanical properties of cortical bone tissue. At the same time, decreasing values of  
46  
47  
48  
49  
50  
51  
52  
53  
54  
55  
56  
57  
58  
59  
60

1  
2  
3 amplitude  $\Delta M$  (Fig. 5B) indicate that the indentation experiment is involving a sufficient  
4 amount of tissue volume such that homogenized material properties are sensed by the  
5 indentation probe. The stabilization of  $M_0$  and the decay to a negligible value of  $\Delta M$  occurs at  
6 approximately the same length scale. This suggests that the homogenization process has  
7 completely developed at approximately 300 nm maximum depth, corresponding to a  $\sim 2 \mu\text{m}$   
8 contact diameter between the tissue and the indenter.  
9

10  
11  
12 Homogenization arguments alone are not able to fully justify the pronounced decay of  
13 the indentation moduli with the penetration depth achieved with the experimental tests,  
14 quantifiable in  $\sim 24\%$  and  $\sim 34\%$  reductions in the axial and transverse directions,  
15 respectively. Instead, the decrease in indentation modulus with indentation depth may be  
16 explained by considering peculiar deformation and failure mechanisms of bone tissue at the  
17 nanostructural level, such as shear transfer between mineral particles via intermediate ductile  
18 organic layers [36], slippage at the collagen–mineral interface [37], phase transformation of  
19 the mineral phase [38], and sacrificial bond disruption between fibrils [39]. In particular,  
20 Gupta and coworkers [40, 41] showed that critical interfacial shear strength between the fibril  
21 and the interfibrillar matrix layer is exceeded when the bone is compressed above the yield  
22 point. When this happens, the matrix flows past the fibrils, resulting in frictional losses and  
23 debonding of the fibrils and extrafibrillar matrix. A further evidence for this mechanism is  
24 achieved considering a single loading-unloading cycle of bone [41], as when a bone sample is  
25 relaxed after being deformed beyond the yield point, irreversible deformations develop at the  
26 tissue level but not at the fibril level. If we compare the loading and unloading stiffnesses at  
27 the tissue level, damage induced decrease in the tissue Young's modulus occurs: this decay,  
28 quantified as  $\sim 20\text{-}25\%$ , is consistent with the progressive diminishing of the stiffness mean  
29 value while increasing the maximum depth evidenced in the present work. Moreover, as the  
30 deformation mechanisms mentioned above contribute in determining a loss of integrity of the  
31  
32  
33  
34  
35  
36  
37  
38  
39  
40  
41  
42  
43  
44  
45  
46  
47  
48  
49  
50  
51  
52  
53  
54  
55  
56  
57  
58  
59  
60



1  
2  
3 tissue, they can be considered as damage phenomena that cause a progressive degradation of  
4 material continuity; we speculate that a damage model can phenomenologically represents  
5 the overall tissue response subject to nanoindentation. Recently, a numerical study performed  
6 by our group [42] was devoted to the investigation of the role played by damage mechanics in  
7 the nanoindentation of osteonal lamellar bone and we showed that damage models can  
8 predict the loss in mechanical properties obtained in the experiments.  
9  
10  
11  
12  
13  
14  
15

16 The results of this work show that the stiffness modulation of the tissue is consistent  
17 with anisotropic fibrillar layers with a specific crystal orientation. Indeed, based on the  
18 difference of the elastic moduli in the directions perpendicular to the fibril ( $E_p$ , see Table 2)  
19 between the thick and this sub-lamellae, it can be speculated that the mineral platelets have an  
20 intrinsic orientation that could play a role in determining the mechanical properties normal to  
21 the fibrils long axis. This observation would agree with the rotated plywood model  
22 introduced by Weiner et al. [33, 34], where collagen fibrils are rotated not only with respect  
23 to the lamellar boundary but also around their own axis (Fig. 8), as the mechanical properties  
24 obtained for a sub-layer can be explained by the azimuthal rotation of the fibrils around the  
25 longitudinal axis  $L$ , which changes the crystal orientation. A further evidence that the  
26 hydroxyapatite crystals strongly influences the elastic properties of the mineralized collagen  
27 fibrils along different directions is provided by Rho et al. [43], who studied intramuscular  
28 herring bones where mineralized collagen fibrils have a single orientation with a variation in  
29 mineralization along the length. Results clearly showed that the anisotropy ratio is influenced  
30 by the mineralization, as it drops from  $\sim 2.1$  in the fully mineralized region to  $\sim 1.1$  in areas at  
31 the earliest stage of mineralization. In this case, the presence of the mineral crystals seems to  
32 be the main aspect responsible for the difference in the elastic properties along different  
33 directions.  
34  
35  
36  
37  
38  
39  
40  
41  
42  
43  
44  
45  
46  
47  
48  
49  
50  
51  
52  
53  
54  
55  
56  
57  
58  
59  
60

1  
2  
3 As already said in the materials and methods section, the bone samples were tested in  
4  
5 ambient conditions. Although samples still retain a significant degree of hydration in this  
6  
7 condition, in general an artificial increase in stiffness and reduction in ductility compared to  
8  
9 the native state could results. However, Hengsberger et al. [44] adopted instrumented  
10  
11 indentation to compare dry and wet samples at different length scales, which are comparable  
12  
13 to the ones investigated here. Basically, what they found is that: (i) thick lamellae exhibited a  
14  
15 significant decrease in indentation modulus with increasing indentation depth, as reported in  
16  
17 this study; (ii) the comparative trends of indentation depth and lamella type were similar for  
18  
19 dry and physiological conditions. Thus the effect of testing dry instead of wet samples seems  
20  
21 the same at multiple length scales. Therefore, relative modulations in mechanical properties  
22  
23 are expected to remain valid, as well as the comparison between the mechanical properties at  
24  
25 the different experimental characteristic length probed and along different directions.  
26  
27 Anyway, future developments will consider the application of the present experimental-  
28  
29 analytical procedure to tests in conditions closer to the physiological.  
30  
31  
32  
33  
34  
35

## 36 5 CONCLUSION

37  
38 In this work, the hierarchical arrangement of lamellar bone was found to be a major  
39  
40 determinant for modulation of mechanical properties and anisotropic mechanical behavior of  
41  
42 the tissue. More in detail:  
43  
44

- 45 • the size effect on lamellar bone anisotropic mechanical behavior, evidenced by the  
46  
47 decline of indentation modulus versus probe size, and the critical length at which  
48  
49 homogenization of the mechanical properties occurs were determined by measuring the  
50  
51 spatial modulation of indentation response;  
52  
53
- 54 • by employing a laminate-composite based analytical model, the elastic constants for a  
55  
56 sub-layer of mineralized collagen fibrils within an osteonal lamella were determined on  
57  
58  
59  
60

1  
2  
3 the basis of their spatial arrangements and were validated through direct comparison of  
4  
5 the experimental indentation moduli and the predicted ones computed by the Swadener-  
6  
7 Pharr model;  
8

9  
10 The structural complexity of bone tissue requires that the assessment of its mechanical  
11  
12 properties involves multiple hierarchical levels, from the macroscopic scale down to the  
13  
14 micro and nanostructural level till the most basic components. Understanding structure-  
15  
16 property relationships and the effects of structural features on the biomechanical properties of  
17  
18 bone would enable not only the development of more accurate models for analysis of  
19  
20 implants and potential bone-replacement materials, but also the progress in designing bio-  
21  
22 inspired structural materials which take advantage of the mechanical design principles found  
23  
24 in nature. These latter topics undoubtedly represent fascinating long-term scientific goals in  
25  
26 the materials science and engineering field.  
27  
28  
29  
30  
31

### 32 **ACKNOWLEDGMENTS**

33  
34 The authors would like to thank the MIT-Italy Program for supporting the research and the  
35  
36 Progetto Rocca for supporting Davide Carnelli's scholarship at the MIT. The DMSE  
37  
38 Nanomechanical Technology Laboratory and the Institute for Soldier Nanotechnologies  
39  
40 (ISN) at the MIT are gratefully acknowledged for use of equipment and facilities. MD  
41  
42 acknowledges support by the ONR Grant N00014-08-1-0510, and by the Advanced Materials  
43  
44 for Micro and Nano Systems Programme of the Singapore-MIT Alliance (SMA).  
45  
46  
47  
48  
49  
50  
51  
52  
53  
54  
55  
56  
57  
58  
59  
60

## REFERENCES

1. Weiner, S. & Wagner, H. D. 1998 The material bone: structure mechanical function relations. *Annu. Rev. Mater. Sci.* **28**, 271-298. (DOI 10.1146/annurev.matsci.28.1.271)
2. Currey, J. D. 2002 *Bones: structure and mechanics*. Princeton, NJ: Princeton University Press.
3. Cowin, S. C. 2001 *Bone mechanics handbook*. Boca Raton, FL: CRC Press Inc.
4. Currey, J. D. 1984 *The mechanical adaptations of bones*. Princeton, NJ: Princeton University Press.
5. Rho, J. Y., Kuhn-Spearing, L. & Zioupos, P., 1998 Mechanical properties and the hierarchical structure of bone. *Med. Eng. Phys.*, **20**, 92-102. (DOI 10.1016/S1350-4533(98)00007-1)
6. Fratzl, P. & Weinkamer, R. 2007 Nature's hierarchical materials. *Progress Mater. Sci.* **52**, 1263-1334. (DOI 10.1016/j.pmatsci.2007.06.001)
7. Fratzl, P., Gupta, H. S., Paschalis, E. P. & Roschger, P. 2004 Structure and mechanical quality of the collagen-mineral nano-composite in bone. *J. Mater. Chem.* **14**, 2115-2123. (DOI 10.1039/B402005G)
8. Fratzl, P. & Gupta, H. S. 2007 *Nanoscale mechanisms of bone deformation and fracture*. Weinheim: Wiley-VCH Verlag GmbH.
9. Wagermaier, W., Gupta, H.S., Gourrier, A., Burghammer, M., Roschger, P. & Fratzl, P. 2006 Spiral twisting of fiber orientation inside bone lamellae. *Biointerph.* **1**, 1-5. (DOI 10.1116/1.2178386)
10. Wagermaier, W., Gupta, H. S., Gourrier, A., Paris, O., Roschger, P., Burghammer, M., Riekel, C. & Fratzl P. 2007 Scanning texture analysis of lamellar bone using microbeam synchrotron x-ray radiation. *J. Appl. Crystall.* **40**, 115-120. (DOI 10.1107/S0021889806044888)

- 1  
2  
3 11. Reilly, D. T. & Burstein, A. H. 1975 The elastic and ultimate properties of compact  
4 bone tissue. *J. Biomech.* **6**, 393-396. (DOI 10.1016/0021-9290(75)90075-5)  
5  
6  
7 12. Ascenzi, A., Baschieri, P. & Benvenuti, A. 1994 The torsional properties of single  
8 selected osteons. *J. Biomech.* **27**, 875-884. (DOI 10.1016/0021-9290(94)90260-7)  
9  
10  
11 13. Ascenzi, A., Ascenzi, M. G., Benvenuti, A. & Mango, F. 1997 Pinching in  
12 longitudinal and alternate osteons during cyclic loading. *J. Biomech.* **30**, 689-695.  
13 (10.1016/S0021-9290(97)00002-X)  
14  
15  
16 14. Rho, J. Y. 1996 An ultrasonic method for measuring the elastic properties of human  
17 tibial cortical and cancellous bone. *Ultrasonics* **34**, 777-783. (DOI 10.1016/S0041-  
18 624X(96)00078-9)  
19  
20  
21 15. Fan, Z., Swadener, J. G., Rho, J. Y., Roy, M. E. & Pharr, G. M. 2002 Anisotropic  
22 properties of human tibial cortical bone as measured by nanoindentation. *J. Orthop. Res.* **20**,  
23 806-810. (DOI 10.1016/S0736-0266(01)00186-3)  
24  
25  
26 16. Rho, J. Y., Currey, J. D., Zioupos, P. & Pharr, G. M. 2001 The anisotropic young's  
27 modulus of equine secondary osteons and interstitial bone determined by nanoindentation. *J.*  
28 *Exp. Biol.* **204**, 1775-1781.  
29  
30  
31 17. Franzoso, G. & Zysset, P.K. 2009 Elastic anisotropy of human cortical bone  
32 secondary osteons measured by nanoindentation. *J. Biomech. Eng.* **131**, 021001.1-021001.11.  
33  
34  
35 18. Yoon, Y. J. & Cowin, S. C. 2008 The estimated elastic constants for a single bone  
36 osteonal lamella. *Biomech. Model. Mechanobiol.* **7**, 1-11. (DOI 10.1007/s10237-006-0072-8)  
37  
38  
39 19. Gupta, H. S., Stachewicz, U., Wagermaier, W., Roschger, P., Wagner, H. D. & Fratzl,  
40 P. 2006 Mechanical modulation at the lamellar level in osteonal bone. *J. Mater. Res.* **21**,  
41 1913-1921. (DOI 10.1557/jmr.2006.0234)  
42  
43  
44 20. Kasiri, S. & Taylor, D. 2008 A critical distance study of stress concentrations in bone.  
45 *J. Biomech.* **41**, 603-609. (DOI 10.1016/j.jbiomech.2007.10.003)  
46  
47  
48  
49  
50  
51  
52  
53  
54  
55  
56  
57  
58  
59  
60

- 1  
2  
3 21. Yao, H., Dao, M., Carnelli, D., Tai, K. & Ortiz, C. 2011 Size-dependent heterogeneity  
4 benefits the mechanical performance of bone. *J. Mech. Phys. Sol.* **59**, 64-74. (DOI  
5 10.1016/j.jmps.2010.09.012)  
6  
7  
8  
9  
10 22. Hofmann, T., Heyroth, F., Meinhard, H., Franzel, W. & Raum, K. 2006 Assessment  
11 of composition and anisotropic elastic properties of secondary osteon lamellae. *J. Biomech.*  
12 **39**, 2282-2294. (DOI 10.1016/j.jbiomech.2005.07.009)  
13  
14  
15  
16 23. Oliver, W. C. & Pharr, G. M. 2004 Measurement of hardness and elastic modulus by  
17 instrumented indentation: Advances in understanding and refinements to methodology. *J.*  
18 *Mater. Res.* **19**, 3-20. (DOI 10.1557/jmr.2004.19.1.3)  
19  
20  
21  
22 24. Tai, K., Qi, H. J. & Ortiz, C. 2005 Effect of mineral content on the nanoindentation  
23 properties and nanoscale deformation mechanisms of bovine tibial cortical bone. *J. Mater.*  
24 *Sci.: Mater. Med.* **16**, 947-959. (DOI 10.1007/s10856-005-4429-9)  
25  
26  
27  
28  
29 25. Oliver, W. C. & Pharr, G. M. 1992 An improved technique for determining hardness  
30 and elastic modulus using load and displacement sensing indentation experiments. *J. Mater.*  
31 *Res.* **7**, 1564-1583. (DOI 10.1557/JMR.1992.1564)  
32  
33  
34  
35  
36 26. Currey, J. D. 1969 The relationship between the stiffness and the mineral content of  
37 bone. *J. Biomech.* **2**, 477-480. (DOI 10.1016/0021-9290(69)90023-2)  
38  
39  
40  
41 27. Seto, J., Gupta, H. S., Zaslansky, P., Wagner, H. D. & Fratzl, P. 2008 Tough lessons  
42 from bone: extreme mechanical anisotropy at the mesoscale. *Adv. Funct. Mater.* **18**, 1905-  
43 1911. (DOI 10.1002/adfm.200800214)  
44  
45  
46  
47 28. Fritsch, A. & Hellmich, C. 2007 Universal microstructural patterns in cortical and  
48 trabecular, extracellular and extravascular bone materials: micromechanics-based prediction  
49 of anisotropic elasticity. *J. Theoret. Biol.* **244**, 597-620. (DOI 10.1016/j.jtbi.2006.09.013)  
50  
51  
52  
53  
54  
55  
56  
57  
58  
59  
60

- 1  
2  
3 29. Hellmich, C. & Ulm, F. J. 2002 Are mineralized tissues open crystal foams reinforced  
4 by crosslinked collagen?-some energy arguments. *J. Biomech.* **35**, 1199-1212. (DOI  
5 10.1016/S0021-9290(02)00080-5)  
6  
7  
8  
9  
10 30. Hellmich, C., Barthélémy, J-F. & Dormieux, L. 2004 Mineral-collagen interactions in  
11 elasticity of bone ultrastructure-a continuum micromechanics approach. *Eur. J. Mech. -*  
12 *A/Solids* **23**, 783-810. (DOI 10.1016/j.euromechsol.2004.05.004)  
13  
14  
15  
16 31. Delafargue, A. & Ulm, F.J. 2004 Explicit approximations of the indentation modulus  
17 of elastically orthotropic solids for conical indenters. *Int. J. Solids Struct.* **41**, 7351-7360.  
18 (DOI 10.1016/j.ijsolstr.2004.06.019)  
19  
20  
21  
22  
23 32. Swadener, J. G. & Pharr, G.M. 2001 Indentation of elastically anisotropic half-spaces  
24 by cones and paraboloids of revolution. *Phil. Mag. A* **81**, 447-466. (DOI  
25 10.1080/01418610108214314)  
26  
27  
28  
29 33. Weiner, S., Arad, T., Sabanay, I. & Traub, W. 1997 Rotated plywood structure of  
30 primary lamellar bone in the rat: orientations of the collagen fibril arrays. *Bone* **20**, 509-514.  
31 (DOI 10.1016/S8756-3282(97)00053-7)  
32  
33  
34  
35 34. Weiner, S., Traub, W. & Wagner, H. D. 1999 Lamellar bone: structure-function  
36 relations. *J. Struct. Biol.* **126**, 241-255. (DOI 10.1006/jsbi.1999.4107)  
37  
38  
39  
40 35. Akiva, U., Wagner, H. D. & Weiner, S. 1998 Modelling the three-dimensional elastic  
41 constants of parallel-fibred and lamellar bone. *J. Mater. Sci.* **33**, 1497-1509. (DOI  
42 10.1023/A:1004303926771)  
43  
44  
45  
46 36. Jager, I. & Fratzl, P. 2000 Mineralized collagen fibrils: a mechanical model with a  
47 staggered arrangement of mineral particles. *Biophys. J.* **79**, 1737-1746. (DOI 10.1016/S0006-  
48 3495(00)76426-5)  
49  
50  
51  
52  
53  
54  
55  
56  
57  
58  
59  
60

- 1  
2  
3 37. Mercer, C., He, M. Y., Wang, R. & Evans, A.G. 2006 Mechanisms governing the  
4 inelastic deformation of cortical bone and application to trabecular bone. *Acta Bio.* **2**, 59-68.  
5  
6 (DOI 10.1016/j.actbio.2005.08.004)  
7  
8  
9  
10 38. Carden, A., Rajachar, R.M., Morris, M.D. & Kohn, D. H. 2003 Ultrastructural  
11 changes accompanying the mechanical deformation of bone tissue: a raman imaging study.  
12  
13 *Calcif. Tissue Int.* **72**, 166-175. (DOI 10.1007/s00223-002-1039-0)  
14  
15  
16 39. Fantner, G., Hassenkam, T., Kindt, J. H., Weaver, J. C., Birkedal, H., Pechenik, L.,  
17  
18 Cutroni, J. A., Cidade, G. A. G., Stucky, G. D., Morse, D. E. & Hansma, P.K. 2005  
19  
20 Sacrificial bonds and hidden length dissipate energy as mineralized fibrils separate during  
21  
22 bone fracture. *Nat. Mater.* **4**, 612-616. (DOI 10.1038/nmat1428)  
23  
24  
25 40. Gupta, H. S., Wagermaier, W., Zickler, G. A., Aroush, D. R. B., Funari, S. S.,  
26  
27 Roschger, P., Wagner, H. D. & Fratzl, P. 2005 Nanoscale deformation mechanisms in bone.  
28  
29 *Nano Lett.* **5**, 2108-2111. (DOI 10.1021/nl051584b)  
30  
31  
32 41. Gupta, H. S., Wagermaier, W., Zickler, G. A., Hartmann, J., Funari, S. S., Roschger,  
33  
34 P., Wagner, H.D. & Fratzl, P. 2006 Fibrillar level fracture in bone beyond the yield point. *Int.*  
35  
36 *J. Fracture* **139**, 425-436. (DOI 10.1007/s10704-006-6635-y)  
37  
38  
39 42. Lucchini, R., Carnelli, D., Ponzoni, M., Bertarelli, E., Gastaldi, D. & Vena, P. 2011  
40  
41 Role of damage mechanics in nanoindentation of lamellar bone at multiple sizes: experiments  
42  
43 and numerical modeling. *J. Mech. Behav. Biomed. Mater.* **4**, 1852-1863. (DOI  
44  
45 10.1016/j.jmbbm.2011.06.002)  
46  
47  
48 43. Rho, J. Y., Mishra, S. R., Chung, K., Bai, J. & Pharr, G. M. 2001 Relationship  
49  
50 between ultrastructure and the nanoindentation properties of intramuscular herring bones.  
51  
52 *Annals Biomed. Eng.* **29**, 1082-1088. (DOI 10.1114/1.1424913)  
53  
54  
55  
56  
57  
58  
59  
60



1  
2  
3 44. Hengsberger, S., Kulik, A. & Zysset, P. 2002 Nanoindentation discriminates the  
4  
5 elastic properties of individual human bone lamellae under dry and physiological conditions.  
6

7 *Bone* **30**, 178-184. (DOI 10.1016/S8756-3282(01)00624-X)  
8  
9  
10  
11  
12  
13  
14  
15  
16  
17  
18  
19  
20  
21  
22  
23  
24  
25  
26  
27  
28  
29  
30  
31  
32  
33  
34  
35  
36  
37  
38  
39  
40  
41  
42  
43  
44  
45  
46  
47  
48  
49  
50  
51  
52  
53  
54  
55  
56  
57  
58  
59  
60

For Review Only

**FIGURES**

**Figure 1.** (A) Optical microscopy image of osteonal bovine bone tissue parallel to the osteonal axis (axial direction). (B) Optical microscopy image of osteonal bovine bone tissue normal to the osteonal axis (transverse direction). (C) Scanning electron microscopy image of a region surrounding an individual osteon parallel to the osteonal axis. (D) Home built sample stage enabling the testing of two orthogonal orientations within the same osteon. (E) Illustration of the indentation test directions ( $A$  and  $T_1$ ) with respect to the osteonal microstructure (in red).

**Figure 2.** Averaged load vs. penetration depth plots in the axial (A) and transverse (B) directions at the four tested maximum depths. Error bars are  $\pm$  one standard deviation calculated at 50% of the maximum load during the unloading curve ( $n=363$  for 50 nm maximum depth tests,  $n=273$  for 100 nm maximum depth tests,  $n=189$  for 200 and 300 nm maximum depth tests).

**Figure 3.** Spatial dependence of indentation modulus at 50 (A), 100 (B), 200 (C) and 300 (D) nm maximum penetration depth for axial experiments (parallel to the osteonal axis). Radial distance ( $r$ ) begins at the Haversian canal edge. Each data point represents the mean value and standard deviation of a total of  $n=9$  measurements. The fitting to the oscillatory function of Eq. (1) is shown in each plot (dashed line). The coefficient of determination ( $R^2$ ) values are 0.60 (A), 0.59 (B), 0.59 (C), and 0.01 (D). Note ordinate does not start at zero.

**Figure 4.** Spatial dependence of indentation modulus at 50 (A), 100 (B), 200 (C) and 300 (D) nm maximum penetration depth for transverse experiments (normal to the osteonal axis). Radial distance ( $r$ ) begins at the Haversian canal edge. Each data point represents the mean

1  
2  
3 value and standard deviation of a total of  $n=9$  measurements. The fitting to the oscillatory  
4 function of Eq. (1) is shown in each plot (dashed line). The coefficient of determination ( $R^2$ )  
5 values are 0.61 (A), 0.58 (B), 0.61 (C), and 0.01 (D). Note ordinate does not start at zero.  
6  
7  
8  
9

10  
11 **Figure 5.** Indentation modulus mean value (A) and amplitude (B) trends with respect to  
12 penetration depth in the axial and transverse directions calculated from Eq. (1). Standard  
13 deviations refer to  $n=9$  measurements.  
14  
15  
16

17  
18  
19  
20 **Figure 6.** Spatial modulation (bars) of the uniaxial elastic moduli  $E$  obtained by using the  
21 Delafargue-Ulm approach [31] at 50 nm maximum penetration depth in the axial (A) and  
22 transverse (B) directions. Maxima correspond to  $E_L$  (longitudinal to collagen fibril long axis)  
23 and minima correspond to  $E_P$  (transverse to collagen fibril long axis). Standard deviations  
24 refer to  $n=9$  measurements. Fitting with the analytical model in Eq. (2) is also shown: the  
25 fitting results, together with the coefficient of determination values  $R^2$ , are reported in Table  
26  
27  
28  
29  
30  
31  
32  
33  
34  
35  
36  
37  
38  
39  
40  
41  
42  
43  
44  
45  
46  
47  
48  
49  
50  
51  
52  
53  
54  
55  
56  
57  
58  
59  
60  
2. Note ordinate does not start at zero.

61  
62  
63  
64  
65  
66  
67  
68  
69  
70  
71  
72  
73  
74  
75  
76  
77  
78  
79  
80  
81  
82  
83  
84  
85  
86  
87  
88  
89  
90  
91  
92  
93  
94  
95  
96  
97  
98  
99  
100  
**Figure 7.** Comparison between the indentation moduli trends obtained experimentally (bars)  
and the ones computed with the Swadener-Pharr method [32] (dots) with a  $\sim 140$  nm spacing  
in the axial (A) and transverse (B) directions. The fitting to the oscillatory function of Eq. (1)  
(dashed line) is shown as well. The input parameters for the Swadener-Pharr method are  
reported in Tables 2-3 for transversely isotropic (TI) and orthotropic (ORTH) material  
models, respectively. In the axial direction (A), the coefficient of determination  $R^2$  values are  
0.59 and 0.60 for the transversely isotropic and orthotropic model, respectively; whereas, in  
the transverse direction (B),  $R^2$  values are 0.62 and 0.61 for the transversely isotropic and  
orthotropic model, respectively. Note ordinate does not start at zero.

1  
2  
3  
4  
5 **Figure 8.** Schematic illustration of the organization of mineralized collagen fibrils and the  
6  
7 plate-shaped mineral crystals within the fibrils in a lamellar unit of osteonal bone according  
8  
9 to the rotated plywood model introduced by Weiner et al. [33, 34]. The three local orthogonal  
10  
11 reference axes labeled L,  $P_1$  and  $P_2$  (relative to the axis of an individual mineralized collagen  
12  
13 fibril) are provided. The three global orthogonal reference axes A,  $T_1$  and  $T_2$  (relative to the  
14  
15 osteonal axis) are provided too. Not drawn to scale.  
16  
17  
18  
19  
20  
21  
22  
23  
24  
25  
26  
27  
28  
29  
30  
31  
32  
33  
34  
35  
36  
37  
38  
39  
40  
41  
42  
43  
44  
45  
46  
47  
48  
49  
50  
51  
52  
53  
54  
55  
56  
57  
58  
59  
60

For Review Only

1  
2  
3  
4  
5  
6  
7  
8  
9  
10  
11  
12  
13  
14  
15  
16  
17  
18  
19  
20  
21  
22  
23  
24  
25  
26  
27  
28  
29  
30  
31  
32  
33  
34  
35  
36  
37  
38  
39  
40  
41  
42  
43  
44  
45  
46  
47  
48  
49  
50  
51  
52  
53  
54  
55  
56  
57  
58  
59  
60

## TABLES

**Table 1.** Summary of the indentation tests carried out in this work. The procedure explained below has been performed in both the axial (A) and transverse ( $T_1$ ) directions on three secondary osteons.

Number of Indentations rows×columns	Maximum depth	Spacing
41×3	50 nm	0.5 $\mu\text{m}$
31×3	100 nm	1 $\mu\text{m}$
21×3	200 nm	2 $\mu\text{m}$
21×3	300 nm	3 $\mu\text{m}$

**Table 2.** Results of fitting with Eq. (2) [19, 26, 27] independently applied to the 50 nm maximum depth data in terms of uniaxial elastic moduli  $E$  (Fig. 7) in the axial and transverse directions. The  $\nu_{LP}$  values (bold typed) were assumed from [18] to perform the fitting. The coefficient of determination  $R^2$  is given in the last column.

Indentation Direction	$E_L$ [GPa]	$E_P$ [GPa]	$G_{LP}$ [GPa]	$\nu_{LP}$ [-]	$R^2$ [-]
Axial	27.70	22.60	9.26	<b>0.301</b>	0.88
Transverse	26.17	17.98	8.16	<b>0.330</b>	0.86

**Table 3.** Set of orthotropic elastic parameters for a sub-layer of mineralized collagen fibrils within an osteonal lamella, inferred by properly merging the two datasets in the axial and transverse directions reported in Table 2. The  $G_{PIP2}$ ,  $\nu_{PIP2}$ ,  $\nu_{LP1}$ , and  $\nu_{LP2}$  parameters (bold typed) were assumed from [18]. For comparison purposes, the set of orthotropic elastic parameters for one sub-layer of the lamellar unit obtained by Yoon and Cowin [18] is reported also. The relationships  $E_L > E_{P2} > E_{P1}$  and  $\nu_{P2P1} > \nu_{P2L} > \nu_{P1L}$  are maintained, as well as  $G_{LP2} > G_{LP1}$ .

	$E_{P1}$ [GPa]	$E_{P2}$ [GPa]	$E_L$ [GPa]	$G_{PIP2}$ [GPa]	$G_{LP1}$ [GPa]	$G_{LP2}$ [GPa]	$\nu_{PIP2}$ [-]	$\nu_{P2P1}$ [-]	$\nu_{P1L}$ [-]	$\nu_{P2L}$ [-]	$\nu_{LP1}$ [-]	$\nu_{LP2}$ [-]
Present work	17.98	22.60	26.94	<b>7.2</b>	8.16	9.26	<b>0.334</b>	0.420	0.220	0.253	<b>0.330</b>	<b>0.301</b>
Yoon, Cowin	16.40	18.07	22.80	7.2	7.1	8.4	0.334	0.381	0.237	0.247	0.330	0.301

**Table 4.** Comparison between the indentation moduli mean value and amplitude of the modulation calculated with the oscillatory function in Eq. (1) and computed by the Swadener-Pharr method [32] in the axial and transverse direction. Percentage discrepancies are calculated as  $e_{M0} = |M_0^{COM} - M_0^{EQ.1}| / M_0^{EQ.1}$  and  $e_{\Delta M} = |\Delta M^{COM} - \Delta M^{EQ.1}| / \Delta M^{EQ.1}$ . The transversely isotropic material model is used.

<b>Indentation Direction</b>	$M_0^{EQ.1}$ [GPa]	$M_0^{COM}$ [GPa]	$\Delta M^{EQ.1}$ [GPa]	$\Delta M^{COM}$ [GPa]	$e_{M0}$ %	$e_{\Delta M}$ %
Axial	26.19	27.00	2.48	2.97	3.07	19.76
Transverse	23.56	23.15	5.53	5.01	-1.78	-9.40

**Table 5.** Comparison between the indentation moduli mean value and amplitude of the modulation calculated with the oscillatory function in Eq. (1) and computed by the Swadener-Pharr method [32] in the axial and transverse direction. Percentage discrepancies are calculated as in Table 4. The orthotropic material model is used.

<b>Indentation Direction</b>	$M_0^{EQ.I}$ [GPa]	$M_0^{COM}$ [GPa]	$\Delta M^{EQ.I}$ [GPa]	$\Delta M^{COM}$ [GPa]	$e_{M0}$ %	$e_{\Delta M}$ %
Axial	26.19	25.80	2.48	2.43	-1.51	-2.02
Transverse	23.56	24.13	5.53	5.77	2.38	4.34

## LIST OF SYMBOLS

$A$	axial indentation direction w.r.t. the global coordinate system
$A, T_1, T_2$	global coordinate system (osteons)
$a_1, a_2$	semi-axes lengths of the elliptical projected area of contact
$\mathbf{a}_1, \mathbf{a}_2, \mathbf{a}_3$	indentation coordinate system for the Swadener-Pharr model
$\mathbf{B}$	Barnett-Lothe tensor
$\mathbf{C}$	stiffness tensor
$C_{ijkl}$	stiffness tensor coefficients
$E$	uniaxial Young's modulus
$E_L$	uniaxial Young's modulus along the mineralized collagen fibrils long axis direction
$E_P$	uniaxial Young's modulus perpendicular to the mineralized collagen fibril long axis for a transversely isotropic material model
$E_{P1}, E_{P2}$	uniaxial Young's moduli perpendicular to the mineralized collagen fibril long axis for an orthotropic material model
$G_{LP}$	shear modulus for a mineralized collagen fibril in the L-P plane for a transversely isotropic material model
$G_{LP1}, G_{LP2}, G_{P1P2}$	shear moduli for a mineralized collagen fibril in the L-P <sub>1</sub> , L-P <sub>2</sub> and P <sub>1</sub> -P <sub>2</sub> planes for an orthotropic material model
$L$	longitudinal indentation direction w.r.t. the local coordinate system
$L, P_1, P_2$	local coordinate system (mineralized collagen fibrils)
$M$	indentation modulus
$M_A$	indentation modulus in the axial direction
$M_T$	indentation modulus in the transverse direction
$M_0$	oscillatory function mean value
$M^{exp}$	experimental indentation modulus
$M^{comp}$	indentation modulus computed with the Swadener-Pharr method
$P$	perpendicular indentation direction w.r.t. the local coordinate system
$T$	transverse indentation direction w.r.t. the global coordinate system
$r$	radial position across the osteon
$r_i$	locations corresponding to the peaks and valleys of the stiffness modulation in the axial and transverse directions
$\mathbf{r}, \mathbf{s}, \mathbf{t}$	orthogonal reference system for the Swadener-Pharr model
$w$	lamellar width
$\gamma$	angle between the direction $\mathbf{t}$ and the $\mathbf{a}_1$ axis
$\Delta M$	oscillatory function amplitude
$\theta$	angle between the long axis of the mineralized collagen fibrils and the loading direction
$\nu_{LP}, \nu_{PP}$	Poisson's ratios for a mineralized collagen fibril in the L-P and perpendicular (PP) planes for a transversely isotropic material model
$\nu_{P1L}, \nu_{P2L}, \nu_{P2P1}, \nu_{LP1}, \nu_{LP2}, \nu_{P1P2}$	Poisson's ratios for a mineralized collagen fibril in the L-P <sub>1</sub> , L-P <sub>2</sub> and P <sub>1</sub> -P <sub>2</sub> planes for an orthotropic material model



**SHORT TITLE**

Mechanical Modulation in Cortical Bone

For Review Only

1  
2  
3  
4  
5  
6  
7  
8  
9  
10  
11  
12  
13  
14  
15  
16  
17  
18  
19  
20  
21  
22  
23  
24  
25  
26  
27  
28  
29  
30  
31  
32  
33  
34  
35  
36  
37  
38  
39  
40  
41  
42  
43  
44  
45  
46  
47  
48  
49  
50  
51  
52  
53  
54  
55  
56  
57  
58  
59  
60

1  
2  
3  
4  
5  
6  
7  
8  
9  
10  
11  
12  
13  
14  
15  
16  
17  
18  
19  
20  
21  
22  
23  
24  
25  
26  
27  
28  
29  
30  
31  
32  
33  
34  
35  
36  
37  
38  
39  
40  
41  
42  
43  
44  
45  
46  
47  
48  
49  
50  
51  
52  
53  
54  
55  
56  
57  
58  
59  
60

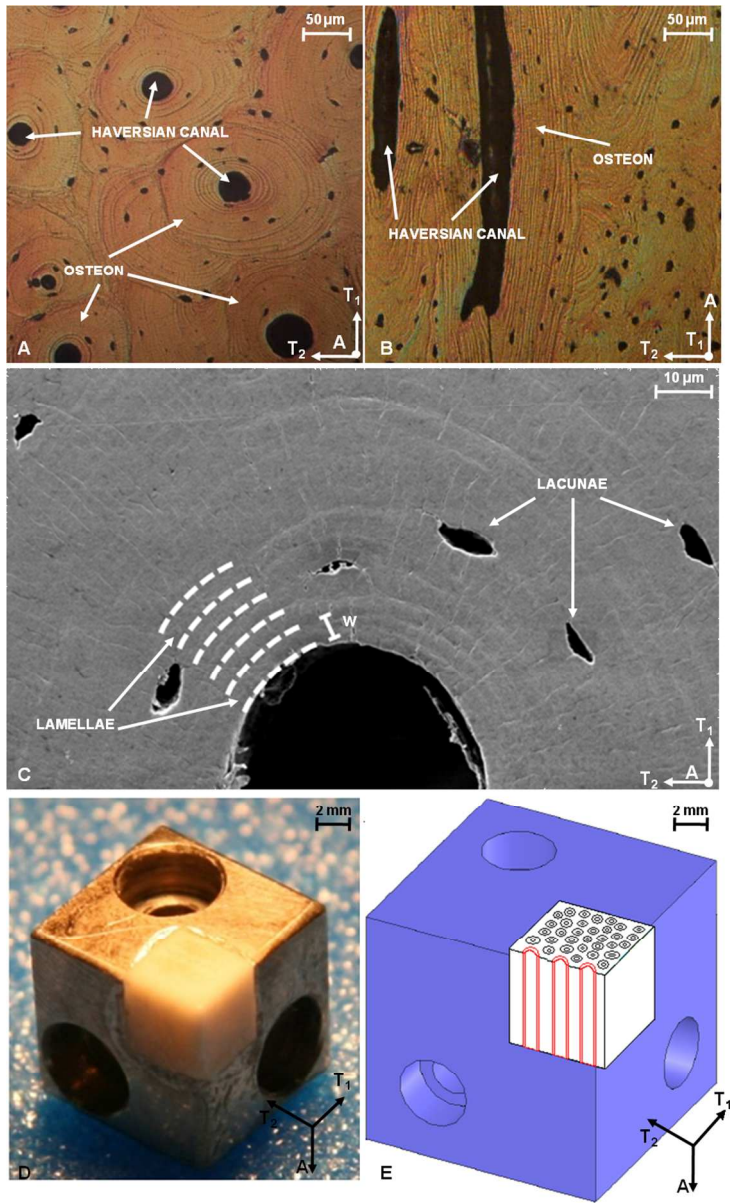
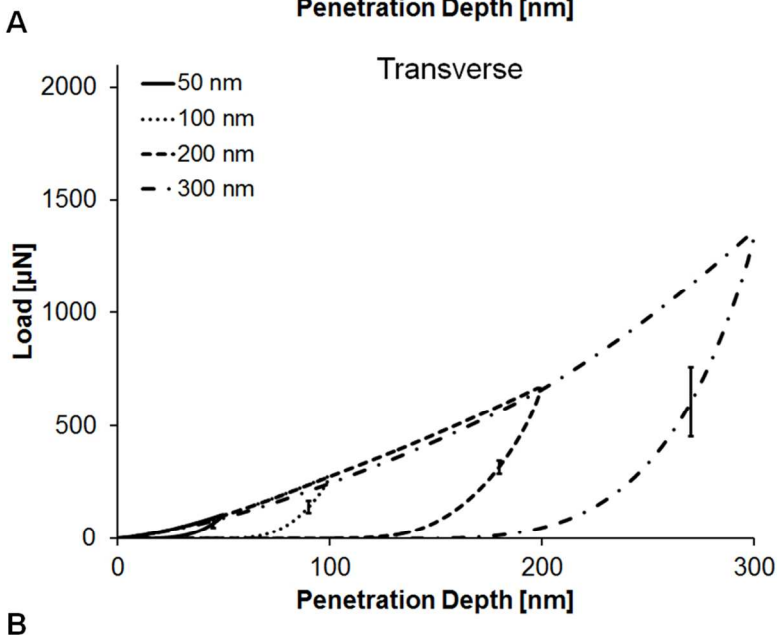
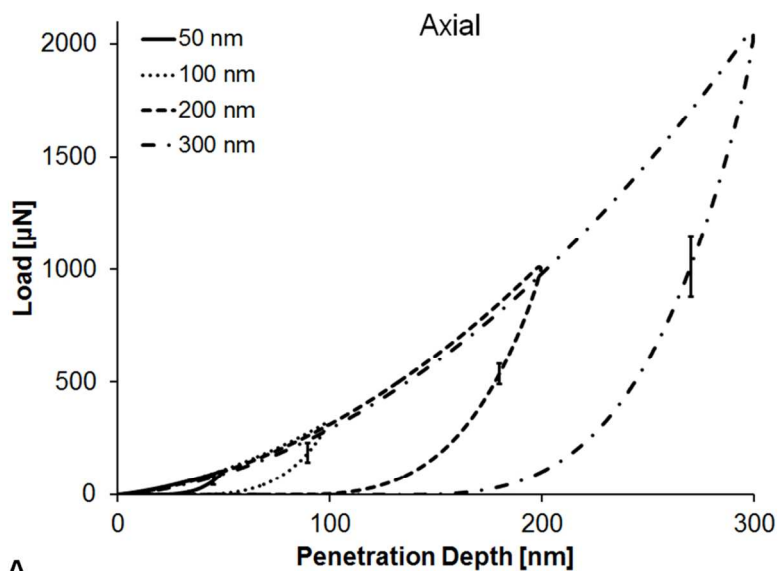


Figure 1  
353x570mm (72 x 72 DPI)



45  
46  
47  
48  
49  
50  
51  
52  
53  
54  
55  
56  
57  
58  
59  
60

Figure 2  
363x533mm (72 x 72 DPI)

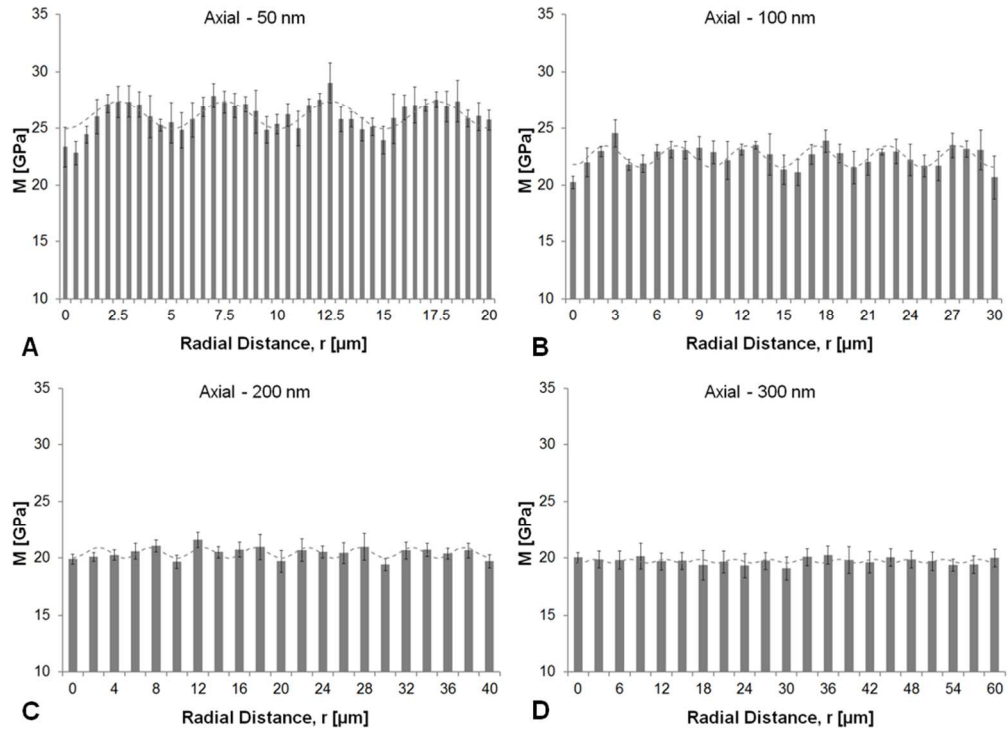


Figure 3  
398x292mm (72 x 72 DPI)

View Only

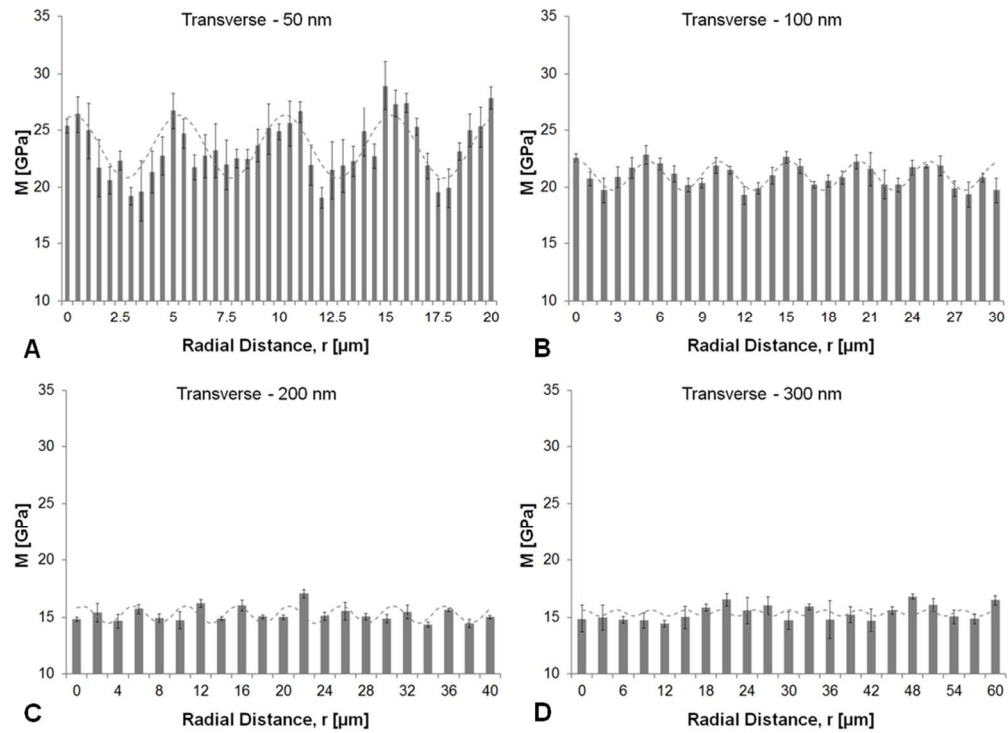


Figure 4  
398x292mm (72 x 72 DPI)

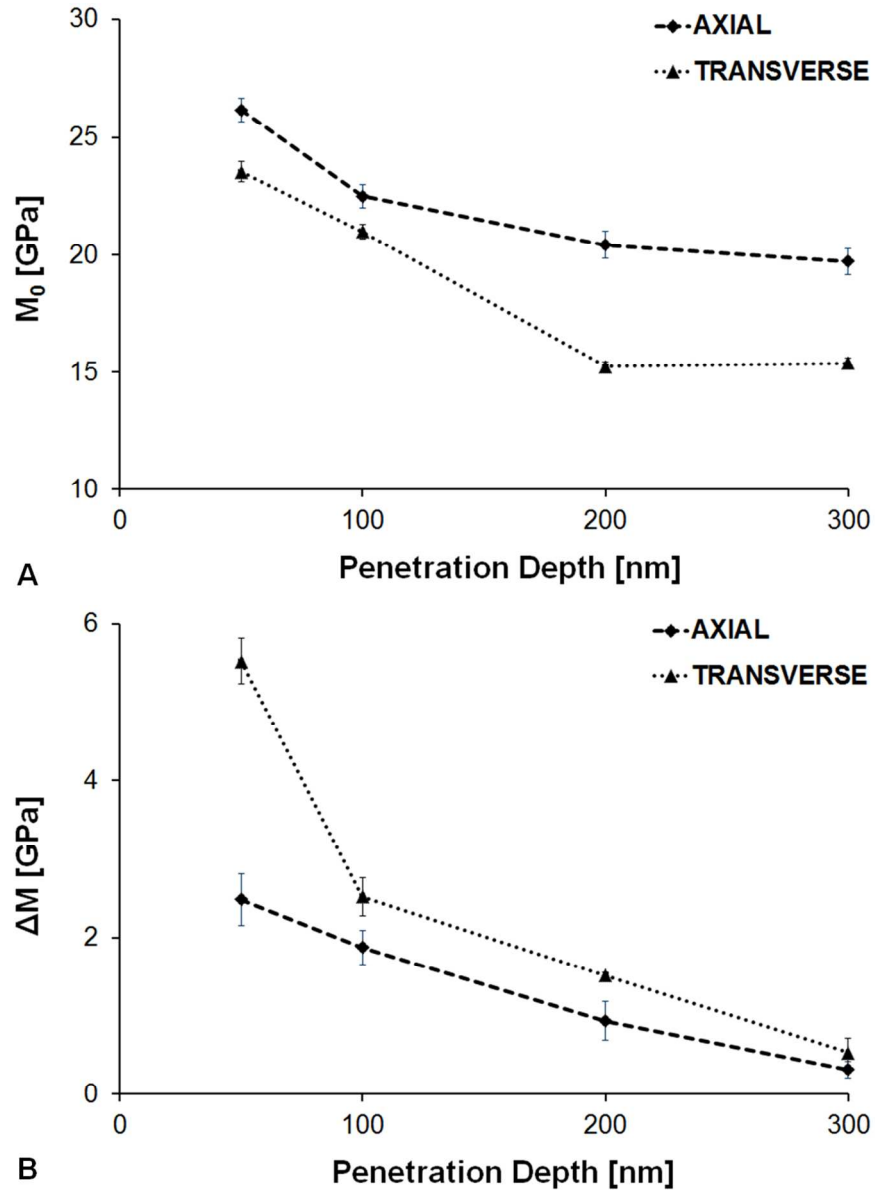


Figure 5  
392x534mm (72 x 72 DPI)

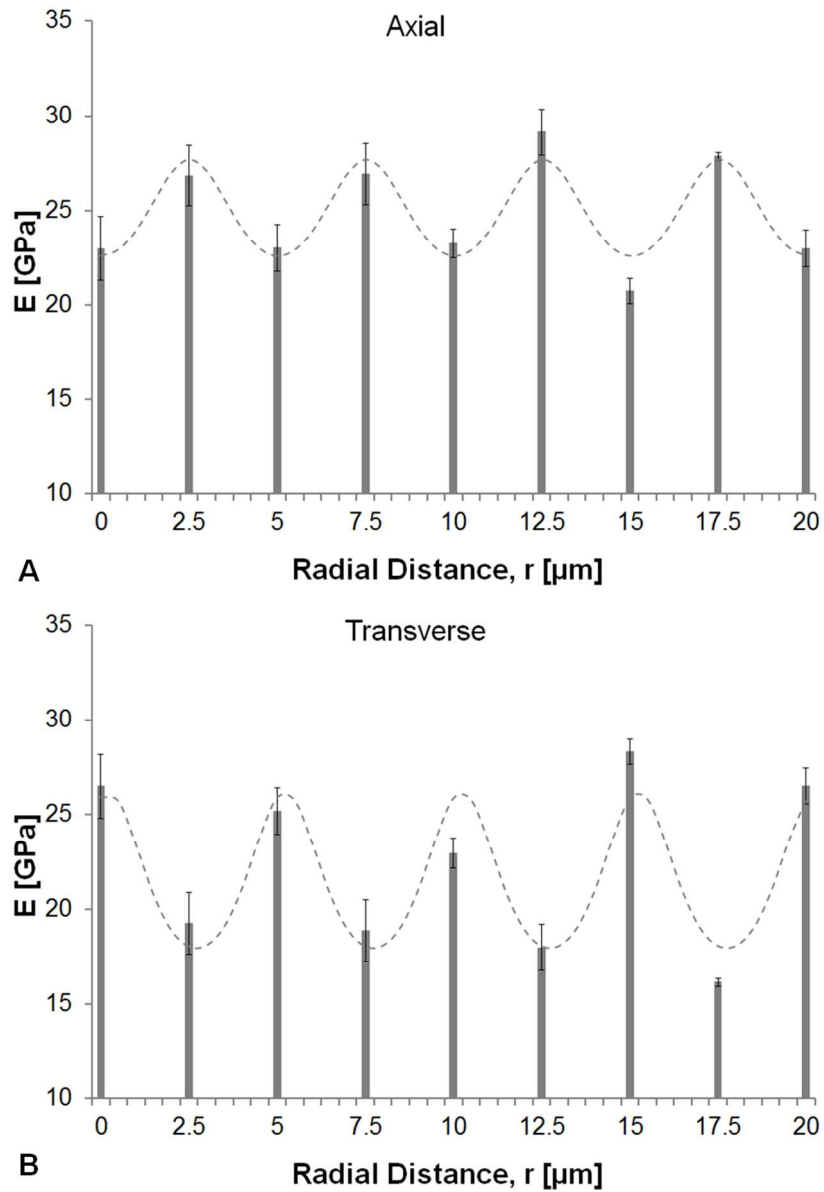


Figure 6  
368x534mm (72 x 72 DPI)

1  
2  
3  
4  
5  
6  
7  
8  
9  
10  
11  
12  
13  
14  
15  
16  
17  
18  
19  
20  
21  
22  
23  
24  
25  
26  
27  
28  
29  
30  
31  
32  
33  
34  
35  
36  
37  
38  
39  
40  
41  
42  
43  
44  
45  
46  
47  
48  
49  
50  
51  
52  
53  
54  
55  
56  
57  
58  
59  
60

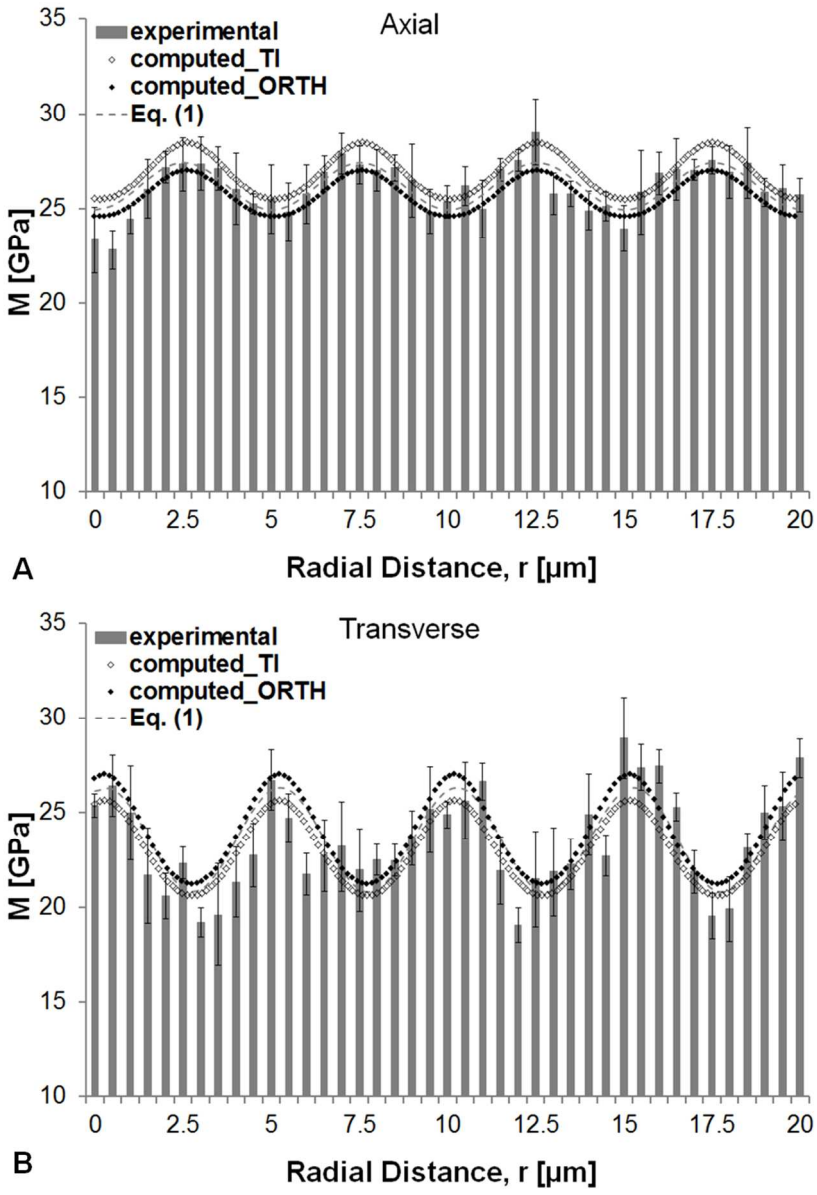


Figure 7  
368x534mm (72 x 72 DPI)



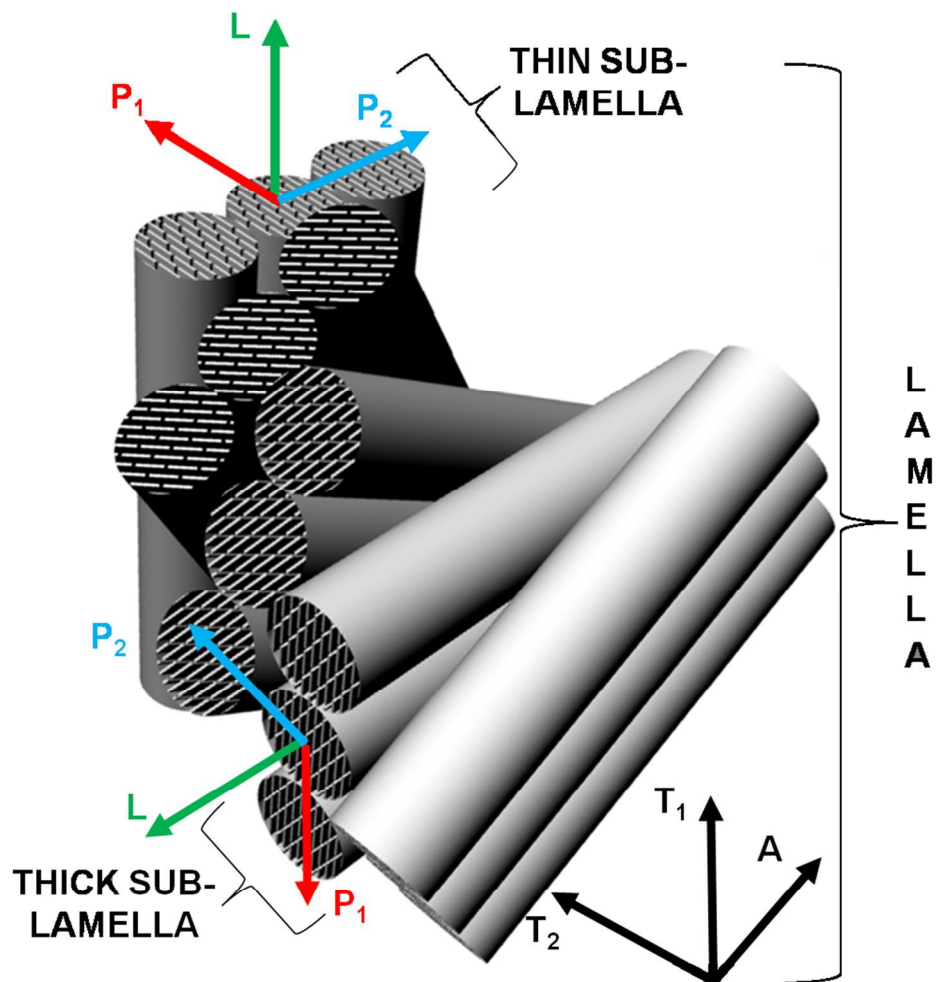


Figure 8  
376x375mm (72 x 72 DPI)



1  
2  
3 Referee: 1

4 Comments to the Author

5 The authors have addressed all the issues raised in my original review. While  
6 the paper is of publishable quality at this point, there are a few small details they  
7 may choose to address before sending the MS to the publisher.  
8

9  
10 1. The AFM RMS roughness values seem to be drawn from images that are 30  
11  $\mu\text{m}$  X 30  $\mu\text{m}$  in area. Assuming the standard 512X512 pixel image, this means  
12 each pixel is 59 nm X 59 nm. Stating an rms roughness of 6 nm in this case is  
13 problematic. For example, if there were oscillations in the surface that were 10  
14 nm in amplitude with a 10 nm period, these would likely sum to an rms of  
15 substantially less than 10 nm when integrated over 6 periods. In short, the rms  
16 roughness is not dependent only on the z accuracy of the measurement; it is also  
17 coupled with the x,y measurements.  
18

19 We thank the reviewer for the suggestion. We will perform further imaging at  
20 higher spatial resolution to confirm the obtained value. In addition, since the  
21 penetration depths achieved in the shallowest experiments is 10 times the  
22 measured roughness, we expect that uncertainty on the roughness estimation  
23 has a little effect on our results.  
24

25  
26 2. The new text in section 2.1 utilizes one set of units in the body text (mN) and  
27 another in the figure caption (fig. 2, ( $\mu\text{N}$ )). This is confusing to the reader.

28 The values of the mean value and standard deviation of maximum load at 50,  
29 100, 200, and 300 in the axial and transverse directions have been reported in  
30  $\mu\text{N}$  to be consistent with Fig. 2.  
31

32  
33 3. In section four when the MS refers to 10-20 fibrils fitting in a 2  $\mu\text{m}$  contact  
34 patch, the authors are limiting themselves to a one dimensional analysis. If they  
35 compute the total area in a 2  $\mu\text{m}$  X 2  $\mu\text{m}$  contact patch and then the total number  
36 of fibrils accommodated in this area, I think they will find that there are  $\sim 10\text{X}$   
37 more fibrils being probed.  
38

39 We agree with the reviewer regarding this observation. The sentence has been  
40 modified as: "the largest experimental characteristic length sampled (300 nm  
41 maximum depth,  $\sim 2.0$   $\mu\text{m}$  contact diameter) may accommodate  $\sim 10$  to 20  
42 bunches of collagen fibrils oriented along multiple directions and, thus, involves  
43 multiple sub-layers..."  
44

45 I found it a bit disheartening that, when confronted with arguments supported  
46 by publications in well regarded journals, the authors choose not to substantially  
47 address the issues of collagen fibril anisotropy and the importance of water in  
48 determining the mechanical properties of bone. These are cutting edge issues  
49 that have been given substantial attention in the last five years or so. However, if  
50 the authors choose to allow these counter arguments to be addressed by others  
51 rather than in this manuscript, I can not in good conscience recommend holding  
52 up publication of the current work.  
53

54 We are sorry if the reviewer wasn't completely satisfied in the way we dealt with  
55 this particular issue in the present paper and in our answer in the previous  
56 response to reviewers. We would just like to underline that some other  
57 considerations about hydrated/not hydrated properties of bone tissue can be  
58  
59  
60

1  
2  
3 found in our previous papers on this topic, and in particular in: Carnelli et al.,  
4 ASME-Journal of Biomechanical Engineering, 2010, 132, 081008.1-081008.10;  
5 Carnelli et al., Journal of Biomechanics, 2011, 44, 1852–1858; and Lucchini et al.,  
6 Journal of the Mechanical Behaviour of Biomedical Materials, 2011, 4, 1852-  
7 1863. We decided not to repeat any of the previously reported considerations in  
8 this new paper.

9  
10 Nevertheless, we agree with the reviewer that the effect of water in determining  
11 the mechanical properties of bone is an important issue in the field of bone  
12 tissue and we will pay even more attention to this particular topic in the near  
13 future.  
14

15  
16  
17  
18 Note to the Editor:

19 Please notice that some of the affiliations have been modified in the current  
20 version of the manuscript.  
21  
22  
23  
24  
25  
26  
27  
28  
29  
30  
31  
32  
33  
34  
35  
36  
37  
38  
39  
40  
41  
42  
43  
44  
45  
46  
47  
48  
49  
50  
51  
52  
53  
54  
55  
56  
57  
58  
59  
60